Research Article

Novel Lanthanum Doped Magnetic Teff Straw Biochar Nanocomposite and Optimization Its Efficacy of Defluoridation of Groundwater Using RSM: A Case Study of Hawassa City, Ethiopia

Temesgen Abeto Amibo [iD],[1] **Surafel Mustafa Beyan** [iD],[1] **and Tsegaye Markos Damite**[2]

[1]*School of Chemical Engineering, Jimma Institute of Technology, Jimma University, P.O. Box 378, Jimma, Ethiopia*
[2]*Department of Material Science & Engineering, Jimma Institute of Technology, Jimma University, P.O. Box 378, Jimma, Ethiopia*

Correspondence should be addressed to Temesgen Abeto Amibo; temesgen.abeto@ju.edu.et

The problem extent of the large concentration of fluoride ions in drinking water is still a central health issue. In the present study, lanthanum doped magnetic Teff straw biochar (LDMTSB) was developed as a novel adsorbent for removing fluoride ions in the groundwater in Rift-Valley regions, especially Hawassa city, Ethiopia. The synthesized LDMTBC was characterized via FTIR, XRD, SEM, and BET. And, this analysis proposed that multiadsorption techniques such as ligand exchange, precipitations, and electrostatic interaction could be evinced throughout the fluoride ions adsorption process by LDMTSB. The constraints that influence the adsorption efficacy, namely, a dosage of LDMTSB, contact time, pH of the solution, and rotational speed, were analyzed and optimized using the response surface methodology approach. Under the optimum situations, LDMTSB dosage: 3.97 g, contact time: 56.36 min, rotational speed: 591.19 rpm, and pH: 3.968 demonstrate high efficacy of LDMTSB with 98.89% fluoride removal capacity. Further, the quadratic model ($R^2 = 0.9841$) was designated for governing the mathematical process. The LDMTSB was successful in the removal of fluoride ions in the groundwater. This study provides a valuable economical solution for the application of Teff straw.

1. Introduction

Drinkable water is not generally available owing to contamination caused by both natural and human sources [1]. The major cause of water contamination was the fast expansion of industry, mining processes, natural gas extraction, and the natural presence of high amounts of minerals.

The ions calcium (Ca), sodium (Na), potassium (K), sulfate (SO_4^{2-}), magnesium (Mg), chloride (Cl), fluoride ion (F), carbonate (CO_3), and bicarbonate (HCO_3) account for more than 90% of the dissolved solids in groundwater [2]. More than 70% of groundwater from deep wells contains F levels higher than the WHO's drinkable limit. F levels in all hot spring water tests were above the WHO drinkable limit, with the highest value of 57.4 mg/L [3]. These all ions are present in drinkable water in a high amount as it affects the

health of human beings, animals, and aquatic organisms [4, 5]. Fluoride concentrations of more than 1.5 g/L are designated contaminants by the WHO because they impair the life of living things. Excessive fluoride consumption causes serious health problems, such as dental fluorosis, which has a concentration range of 1.5 to 4.0 mg/L, skeletal fluorosis, which has a concentration range of 4.0–10.0 mg/L, and gradually debilitating scourge-skeletal fluorosis, which has a concentration greater than 10 mg/L. Fluoride has a safe level when its concentration is less than 1.5 mg/L, which is necessary to avoid tooth decay and anxiety [6, 7]. More than 200 million people are now suffering from high levels of fluoride concentration in their drinking water, which is caused by fluoride being naturally poisoned in the water [8]. The groundwater containing fluoride ions is abundant in the East African Rift Valley basin, particularly in Hawassa,

Zeway, Shashamane, and Adama. The research of acceptable fluoride treatment procedures is required to lower the content of fluoride in drinking water [9].

Within physical methods, several drinking water treatment techniques were developed and implemented to remove such contaminants by high fluoride concentration. Ion exchange, electrokinetic coagulation, membrane separation processes, and adsorption techniques are the widely utilized methods. Each of which has its cons and pros [10]. Electrokinetic coagulation yields poor outcomes from fluoride removal, meaning that it is not that much applicable method. Membranes are unable to resist severe conditions such as high temperature, reactive environments, and contaminated feed. As a result, industrialists do not prefer them as a separation mechanism [10, 11]. In contrast, adsorption is considered as the preferred method of wastewater treatment as it is a method that is easy and suitable to operate and effective in purifying waste water as it has high efficiency of deodorizing, detoxifying, and easy removal of harmful components from wastewater [11]. Adsorption-based methods use microporous materials that are a very promising cost-efficient technology, which is commonly accepted as the most attractive, efficient, and affordable due to its simple control, low operating and capital investment costs, and higher energy efficiency [12, 13]. The adsorption technique was utilized to decrease the fluorine content in the drinking water for this investigation.

Biochar is prepared through thermal degradation of biomass at moderate temperature by pyrolysis process in the absence of oxygen [14]. Biochar is known for being cheap, safe, and it has a plentiful supplier of raw resources that are used for the production of it such as municipal sludge, livestock manure, and agricultural residues [15]. It also has unique physicochemical characteristics, such as a vast number of pore structures, large specific surface area, stability, and effectiveness. As a result, biochar is ideally suited for use as an adsorbent [16]. Biochar can be prepared from different lignocellulosic materials, and Teff straw can be used for the preparation of magnetic biochar.

Teff straw is a plentiful and indigenous lignocellulose material in Ethiopia, and it is a residual waste obtained after the seeds of Teff were removed. According to Mottaleb and Rahut [17], Ethiopia is a significant producer of Teff in the globe, presently producing a considerable amount of Teff annually in various locations, and Teff accounted for roughly 24% of all grain-cultivated land in Ethiopia in 2017. Teff straw was freely available in all regions of Ethiopia once Teff seeds were removed, and Teff straw was considered a waste [18].

According to Huang et al. [19], to increase the adsorption efficiency, Teff straw biochar can be doped with hydrated metal oxides, such as Zr (IV), La (III), Fe (II), Fe (III), and Ce (IV), that were widely investigated for treatment purposes because it could supply a large number of coordination sites and had a particular affinity for fluoride ions. From those, lanthanum has gotten a lot of interest since it is nontoxic, low-cost, chemically stable, and has an exceptionally high affinity for fluoride even at low concentrations [20].

Up to date, no research has been done on the removal of fluorides ion from groundwater using Teff straw biochar magnetic composite doped with lanthanum. Further, process parameters, namely, adsorption dosage, pH, rotational speed, and adsorption time, that affect the efficiency of the composite on the removal of fluorides was optimized using central composite response surface methodology (RSM-CCD) as a statical tool. RSM-based CCD has been proved as a reliable statical tool to estimate and optimize various variables on removal efficiency [21, 22]. Supplementary characterization of the obtained Teff straw biochar magnetic composite doped with lanthanum by X-ray diffraction (XRD), scanning electron microscope (SEM), Fourier transforms infrared (FTIR), and proximate analysis were executed.

2. Materials and Methods

2.1. Materials and Chemicals Used.
The raw material Eragrostis tef (Teff straw) was collected from Yebu, 10 kilometers from Jimma town, Ethiopia, and high fluoride water content was transported from Hawassa city to Jimma Institute of Technology's Department of Material Science and Engineering to treat and characterize the application, as well as to determine the optimal defloration capacity of the adsorbent. For the current study, ferrous chloride ($FeCl_2 \cdot 4H_2O$), ferric chloride hexahydrate ($FeCl_3 \cdot 6H_2O$), lanthanum chloride ($LaCl_3$), potassium nitrate (KNO_3), hydrochloric acid (HCl), sodium hydroxide (NaOH), sodium chloride (NaCl), ethylenediaminetetraacetic acid (EDTA), and sodium fluoride (NaF) were analytical grade chemicals purchased from Hi-Media Rankem PLC, Addis Ababa, Ethiopia. Distilled water was used throughout this study. The following tools were used to synthesize and characterize the adsorbents: Muffle furnace, sonicator, FTIR (Furrier transmission infrared spectroscope), XRD (X-ray diffraction), TGA (thermogravimetric analysis), BET (Brunauer-Emmett-Teller), and SEM (Scanning Electron Microscope) were employed, as well as UV-spectrophotometer and AAS (atomic absorption spectrophotometer) to test the adsorption of fluoride ions.

2.2. Methods

2.2.1. Biochar Synthesis from Teff Straw (Eragrostis Tef).
Hand-sorting was used to eliminate contaminants such as non-Teff straw, grasses, sand, leaves, and dirt. The Teff straw was then steeped in tap water overnight. The next day, the stocked Teff straw was cleaned three times with distilled water that was produced through the reverse osmosis process. The size of the sun-dried Teff straws was reduced using a knife and other size reduction tools, and the size was analyzed by mesh analysis, and the size between 1 mm and 2 mm was taken, followed by impregnation with diluted (1% v/v) sodium hydroxide to remove the mineral and other impurities from the sample. Then, in the absence of oxygen, it was placed in a muffle furnace at 500°C for 2 hours. After the carbonization process was completed, it was chilled overnight in an L31M muffle furnace. Finally, the Teff straw

biochar was crushed and sieved to achieve a particle size of fewer than 63 μm, which was put on pun and kept in a glass container for later use.

2.2.2. Lanthanum Doped Magnetic Biochar Nanocomposite Adsorbent Preparation.

Teff straw biochar was doped with lanthanum salts to create nanocomposites for adsorption purposes. The chemical coprecipitation technique was utilized to create lanthanum doped magnetic Teff straw biochar [23]. Nanocomposites doped with lanthanum metal salts such as iron salts and lanthanum salts were used to create biochar. Teff straw biochar (8 g) was added to an aqueous solution containing 80 ml of $FeCl_2.4H_2O$ (2.54 g), $FeCl_3 \cdot 6H_2O$ (6.5 g), and $LaCl_3$ (1.96 g), then it was stirred until a homogeneous solution was formed, followed by sonication for further 20 minutes. Following sonication, 1 M sodium hydroxide solution was added to the solution until the pH reached 11 at room temperature. To complete the reaction, the entire mixture was swirled at a rotational speed of 400 rpm at a temperature of 90°C for 1 day, and then it was cooled at room temperature. After cooling, the separation procedure was carried out using Whatman filter paper with a pore size of 42 μm, and the adsorbents were rinsed repeatedly in distilled water until the pH reached seven [24]. Then, the black precipitate was separated through a 42 μm Whatman filter with the help of an external magnet and washed repeatedly with deionized water until the pH decreased to seven. Then, the final precipitate was dried in an oven overnight, followed by calcination in a muffle furnace at 300°C for about two hrs. Finally, the milled lanthanum doped magnetic biochar composite adsorbent was passed through the 1 mm sieve to obtain the constant particle size. To test the adsorption effectiveness of single Teff straw biochar and Teff straw biochar doped with lanthanum, two samples were produced, one without the presence of lanthanum salt and the other with 0.15, 0.2, 0.25, and 0.3 w/w ratios of $LaCl_3$ to biochar. Based on the results of the five trials experiments, magnetic biochar containing lanthanum has better fluoride removal efficiency and was thus chosen for future adsorbent preparation by taking into account previous work on minor changes.

2.3. Characterization of Teff Straw (Eragrostis Tef).

The ASTM (American Society for Testing and Materials) standards were utilized to establish the proximate analysis for moisture content, ash content; volatility contents were examined to estimate the fixed carbon content in Teff straw biomass. The raw Teff straw maintained below 2 mm in thickness weighed 5 grams. The prepared Teff straw was dried in an oven at 1050 degrees Celsius until it formed a uniform mass. The experiment was repeated three times. The ash composition of raw Teff straw ash was determined using a muffle furnace with model number L31M. The 3 g of Teff straw sample was placed in a crucible and burnt at 1000 degrees Celsius until the Teff straw ash was completely transformed to ash. The ash content may be calculated using equation (2). The volatile matter was measured by ASTM (E-872). Then, 2 g of Teff straw samples were burnt in a muffle

furnace with a model number of L31M by using a crucible at 650°C for 6 minutes; hence, it allowed cooling in a desiccator. The volatile matter content was determined by using equation (3). Fixed carbon was determined by subtracting the entire sample content from the sum of the percent moisture, ash, and volatile matter. As a result, the fixed carbon was determined by equation (4)

$$TS_{MC} = \frac{W_B - W_A}{W_B} \times 100\%, \tag{1}$$

where TS_{MC} is the moisture content of raw Teff straw, W_B represents the weight of the Teff straw in its natural state, and W_A represents the weight of the oven-dried sample.

$$TS_{AC} = \frac{W_{C+BA} - W_C}{W_{C+AA} - W_C} \times 100\%, \tag{2}$$

where TS_{AC} is the ash content of Teff straw sample, W_C is the weight of the crucible, W_{C+BA} is the weight of the crucible + sample weight before the ash process, and W_{C+AA} is the weight of the crucible + sample after the ash process.

$$TS_{VC} = \frac{TS_{IW} - TS_{FW}}{TS_{IW}} \times 100\%, \tag{3}$$

where TS_{VC} stands for the volatility content of the Teff straw sample, TS_{IW} stands for the initial weight of the Teff straw sample, and TS_{FW} stands for the final weight of the Teff straw sample.

$$FCC = 100\% - [TS_{MC} + TS_{AC} + TS_{VC}] \times 100\%, \tag{4}$$

where FCC stands for fixed carbon content, TS_{MC} stands for the moisture content of raw Teff straw, TS_{AC} is the ash content of Teff straw samples, TS_{VC} stands for volatility content of Teff straw sample.

2.4. Characterization of Biochar Produced.

The fixed carbon content is ground to produce biochar from Teff straw raw material [25]. Biochar produced characterized by using different types of equipment such as FTIR, XRD, TGA, SEM, yields of biochar obtained from Teff straw, point zero charges were determined.

2.4.1. FTIR Analysis.

FTIR was used to determine the functional groups found in the raw Teff straw, sample, Teff straw biochar, and lanthanum modified Teff straw biochar comparatively. The bond stretching and vibrations of functional groups were studied using an FTIR analyzer at room temperature with a spectrum 400-IR (Perkin Elmer) in the range 4500–400 cm^{-1} and KBr pellets as a reference. The chemical functional groups were then identified by looking at the wavenumbers associated with signals in the FTIR spectra and comparing them to the standard absorbance of functional groups [26].

2.4.2. X-Ray Diffraction (XRD) Analysis.

According to Yao et al. [27], XRD was used to determine the crystallinity index analyses purpose by using crystallinity peak area and

amorphous peak area for Teff straw biochar as well as modified biochar with lanthanum. The device used to conduct X-ray diffraction was the XRD-7000 apparatus for studies on the produced material powder. The studies were carried out with the angle of diffraction (2θ) kept between 10 and 80 degrees. Using the crystallinity index equation, determine if the material is crystalline, semicrystalline, or amorphous.

$$\text{CI} = \frac{A_C}{A_T} \times 100\%, \tag{5}$$

where CI stands the crystallinity index, A_C crystallinity peak area, and A_T the total area obtained from both crystallinity peak area + amorphous peak area.

2.4.3. SEM Analysis.
SEM analysis was performed to examine the changes in the surface morphology of the biochar before and after modification with iron and lanthanum oxide nanoparticles [28].

2.4.4. Thermal Stability Analysis.
The weight loss of the sample was measured using the TGA-4000 Perkin Elmer instrument [29]. This was done with nitrogen gas for all samples. Under the influence of nitrogen gas, the samples were heated from 25°C to 500°C. The nitrogen gas flow rate was 20 ml/min, with a heating rate of 10°C/min. The data from Derivative Thermogravimetric (DTGA) was also taken. This aids in determining the thermal stability of Teff straw biochar as well as the modified biochar.

2.4.5. BET Analysis.
The BET instrument was used to determine the specific surface area of Teff straw biochar, magnetic biochar, and lanthanum doped magnetic biochar. The Brunauer-Emmett-Teller (BET) technique was used to calculate the volume of adsorbed nitrogen gas based on the adsorption and desorption of various gas concentrations at atmospheric pressure and ambient temperature. The three samples were first treated for 1 hour at 230°C to eliminate air and water molecules from the pore. Finally, the samples were tested.

2.4.6. Point Zero Charge Analysis.
Point of zero charges for a concept that a certain substance has a specific pH at which it is neutral. The point of zero charges is the pH value at which the surface is neutral. The solid addition technique was used to study the point of zero charges for biochar and lanthanum doped Teff straw biochar. In eight separate flasks, 500 ml of KNO_3 (0.1 M) with a pH range of 3 to 10 was produced. 45 ml of KNO_3 (0.1 M) was drawn from 500 ml, the pH of the solution was adjusted with drops of 0.1 N NaOH and 0.1 N HCl solutions, and 0.5 g of powdered Teff straw biochar and Modified biochar with lanthanum samples were added to each flask and shaken at room temperature. The final pH of all samples was measured after 2 days and plotted against the pH change; the intersection point of the curve with the line passing through the origin was used as a reference for determining the point of zero charge value.

2.5. Experimental Design.
The response surface approach was analyzed using the design of expert (v.11) software to evaluate the experimental effects. The optimum strategy for optimizing the process variable, namely adsorption dosage, pH, rotational speed, and adsorption time, is the response surface methodology. It was utilized to determine which component had the most impact on adsorption. To answer such problems, the response surface approach central composite design was selected to evaluate linear interaction and quadratic connections between independent and dependent variables during the optimization of fluoride ions removal from the groundwater. The CCD generates 30 data points based on equation (6), comprising 16 factor points, 8 axial points, and 6 center points (Table 1).

To examine the experimental effects, the response surface approach was evaluated using the design of expert (v.11) software. The optimum adsorption efficiency of modified lanthanum doped magnetic Teff straw biochar was calculated using the response surface approach. This study was conducted to discover which components had the most influence on fluoride ion adsorption, allowing researchers to understand which components have the biggest impact on yield.

$$Y = 2^b + 2b + b_c, \tag{6}$$

where Y represents the number of trials done, b represents the number of independent variables, and b_c represents the number of replicates utilized to determine if the abovementioned experiment was accurate or not.

$$M = a_o + \sum_{i=1}^{n} a_i x_i + \sum_{i=1}^{n} a_{ii} x_i^2 + \sum_{i=1}^{n-1} \sum_{j=i+1}^{n} a_{ij} x_{ij}, \tag{7}$$

where M stands for the predicted response of surface methodology. The number n denotes the number of independent factors utilized to optimize the adsorption capacity. Constant coefficients, first-order (linear) coefficients, second-order (quadratic) interaction coefficients, and second-order (quadratic) noninteraction coefficients are all represented by the coefficients a_o, a_i, a_{ii}, a_{ij}.

3. Results and Discussion

3.1. Proximate Analysis of Raw Teff Straw (Eragrostis Tef).
In this section, the proximate analysis was analyzed to determine the fixed carbon contents of Teff straw by using equation (4). Hence, to investigate the ash content, moisture content, and volatile matter content was mandatory to determine the fixed carbon content in Teff straw. According to the study conducted by Bageru and Srivastava [18], the proximate analysis for Teff straw was reported as moisture content of 6.0 to 8.0%, ash content of 3 to 6%, volatile matter of 70 to 80%; also this study had similar results reported by the previous study. For the current study, the proximate analysis performed was presented in Table 2, the same as that reported in a literature review from another study, the ash content, moisture content, and volatility matter had 4.88%, 6.98%, and 73.61%, respectively. Based on this, the result

TABLE 1: Central composite design matrix for defluoridation efficiency.

Run	Independent variable (factors)				Dependent variable (factor)
	Dosage LDMTSB (g/L)	Contact time (min.)	Rotational speed (rpm)	pH	Defluoridation efficiency (%)
1	4	30	600	3	85.94
2	3	45	500	4.5	95.94
3	4	60	400	6	83.46
4	2	60	400	3	81.77
5	3	45	500	4.5	95.91
6	4	60	400	3	93.03
7	2	30	600	6	73.97
8	4	60	600	6	92.95
9	3	45	500	4.5	90.89
10	3	45	700	4.5	91.98
11	2	30	600	3	73.47
12	3	45	500	7.5	78.15
13	4	60	600	3	97.95
14	3	45	500	4.5	95.90
15	3	75	500	4.5	88.58
16	2	60	600	6	82.50
17	2	30	400	6	71.12
18	4	30	400	6	83.23
19	4	30	600	6	87.34
20	4	30	400	3	90.55
21	1	45	500	4.5	69.75
22	3	15	500	4.5	76.46
23	2	60	400	6	71.67
24	3	45	300	4.5	84.83
25	2	30	400	3	78.88
26	3	45	500	1.5	85.76
27	3	45	500	4.5	95.93
28	3	45	500	4.5	95.95
29	2	60	600	3	83.45
30	5	45	500	4.5	90.46

TABLE 2: Proximate analysis experimental results for Teff straw.

Std.	Analysis conducted	Experimental results	Obtained from literature
(1)	Ash content	4.88%	3 to 6%
(2)	Moisture content	6.98%	6.0 to 8.0%
(3)	Volatile matter content	73.61%	70 to 80%
(4)	Fixed carbon content	14.53%.	12–17%
		Experimental result	Bageru and Srivastava [18]

obtained for fixed carbon content was 14.53%. From the total bases, including ash content, moisture content, and volatile matter, the yield of biochar produced from Teff straw was 12.11 percent, while from fixed carbon, the yield was 83.23 percent. This result was obtained at a temperature of 500°C for 120 minutes.

3.2. Teff Straw Biochar and Magnetic Biochar Modified Lanthanum Physiochemical Properties.
When compared to modified biochar containing lanthanum and biochar made from Teff, straw has distinct properties. The bulk densities of Teff straw biochar and lanthanum doped magnetic Teff straw biochar were 0.42 and 0.592 gcm^{-3}, respectively, as indicated in Table 3 for the experimental findings. This indicates that the bulk density of lanthanum doped magnetic Teff straw

biochar was higher than that of Teff straw biochar, owing to the presence of rare Earth metals within it, which increased its density. Similarly, the pH value of Teff straw biochar is higher than that of lanthanum doped biochar. Teff straw biochar was discovered to have a higher hydroxyl group than lanthanum doped Teff straw biochar, which was attributed to the hydroxyl group contained to make it high pH. Point of zero charge value for Teff straw biochar and lanthanum doped Teff straw biochar were 4.3 and 8.1, respectively. Teff straw biochar had a smaller pH surface area for becoming zero than lanthanum doped Teff straw, which was because Teff straw biochar consumes more acid during point zero charge generation. Teff straw biochar had a surface area of 120.61 m^{2}g^{-1}, while lanthanum doped Teff straw biochar had a surface area of 321.52 m^{2}g^{-1}, indicating that lanthanum doped Teff straw biochar has a larger surface area than Teff

TABLE 3: Different biochar physiochemical properties.

Std.	Analysis conducted	Teff straw biochar	Lanthanum doped Teff straw biochar
(1)	Bulk density (gcm^{-3})	0.42	0.592
(2)	pH	10.8	6.3
(3)	pH_{PZC}	4.3	8.1
(4)	Surface area (m^2g^{-1})	120.61	321.52

straw biochar. As a result, modified biochar had greater adsorption effectiveness than nonmodified biochar. Because the modified biochar is a nanocomposite, it has high surface area availability. Teff straw activated carbon ($552.23\,m^2g^{-1}$) has a higher surface area than coffee husk activated carbon, according to another study ($400\,m^2g^{-1}$). Tef straw biochar surface area ($120.61\,m^2g^{-1}$) was higher than coffee husk biochar, as was the case with activated carbon ($90.2\,m^2g^{-1}$). Research conducted by Kong et al. [30] on the removal of phosphate and fluoride using rice lanthanum doped nanocomposite reported that the surface area of the nanocomposite is $123.28\,m^2g^{-1}$. The point zero charge for both TSBC and LDMTSB is shown in Figure 1.

3.3. Characterization Teff Straw BC and Lanthanum Doped Magnetic Teff Straw BC

3.3.1. Crystallinity Index for TSBC and LDMTSB. Figures 2(a) and (b) show how X-ray diffraction (XRD) may be used to determine the crystalline, amorphous, and semicrystalline phases. As illustrated in Figure 2 (a), the lanthanum doped magnetic Teff straw biochar exhibited an amorphous phase due to the random distribution of atoms inside the modified Teff straw biochar. In addition to this, lanthanum doped magnetic Teff straw biochar has crystalline peaks, and its crystallinity index was around 43.45 percent. The lanthanum doped magnetic Teff straw biochar after fluoride adsorption had crystal peaks, as illustrated in Figure 2 (b), due to the presence of metals such as lanthanum and irons in biochar. The total crystallinity index after adsorption is 43.81 percent. This indicates the modified biochar after adsorption was found in the amorphous phase. The metal ions and fluoride ions found in water are absorbed by an active site found in a nanocomposite. Due to this reason, the ions are randomly distributed, which makes the modified biochar after adsorption in the amorphous phase. The metals exhibit crystalline peaks as a result of the crystallinity nature of the metals, and the crystalline peak in modified biochar is owing to this [31]. The peak represented by 24.10°, 37.05°, 45.49°, and 50.61° represents lanthanum peaks. Peaks for iron (II) and (II) were also found in X-RD patterns 45.00°, 64.62°, and 69.47°. The peak found around 22.11, 53.73, and 69.47 represents the peaks for fluoride absorbed.

3.3.2. Functional Group Analysis. From Figure 3(a), the Fourier transmission infrared spectrophotometer (FTIR) spectra of TSBC contained a variety of peaks that begin ion adsorption. The number of peaks detected in TSBC shows the presence of several functional groups within it; these peaks' functional groups were determined using wavenumber (cm^{-1}) and transmittance (percent). The graph of the TSBC spectra shows a large peak bond stretch between 3500 and $3000\,cm^{-1}$, indicating the existence of free and bond hydroxyl (O-H) functional groups bond stretch [32]. The peaks found at 1800 to $1200\,cm^{-1}$ may be ascribed to a strong carboxyl stretch (C=O) stretched at $1294\,cm^{-1}$ [33]. C-H and carboxylic acid may be attributed to the peak at 1465 to $1000\,cm^{-1}$ [34]. Other prominent peaks identified between 1000 and $695\,cm^{-1}$ reflect significant C-O and C=C [34]. The overall surface of biochar is characterized by the presence of several negatively charged functional groups [35]. Similarly, similar results with other biomass-derived biochars have been published regularly. As seen in Figure 3(b), the LDMTSB clearly shows a decrease in hydroxyl, carboxyl, and carbonate functional groups, with the following alteration when compared to Teff straw biochar. However, minor peaks at 3200, 1846, 1675, 1620, 1500, 1440, 692, 621, 556, and $461\,cm^{-1}$ were detected, which can be ascribed to the presence of residual O-H, C-O, and C≡N functional groups. Furthermore, novel bond lengths were discovered at 650 to $500\,cm^{-1}$, which can be ascribed to the existence of the La-O ($621\,cm^{-1}$) and Fe-O ($556\,cm^{-1}$) bonds stretch, respectively. In different studies' findings, the metal oxide bond stretches were found within these ranges [36]. The peak is shown in Figure 3(c), LDMTSB, pecks are removed through the adsorption process. The free O-H, C≡ N, C=O, and other free bonds found in modified biochars then adsorb the fluoride ions prevalent in water, causing some bond stretch to be lost [37]. The bond stretch for hydroxyl was found at about $3200\,cm^{-1}$; OH bond stretch did not exist after the adsorption process. Bond stretch for C=O, C≡N, and C-O accessible about $1635\,cm^{-1}$, $1410\,cm^{-1}$, $2951\,cm^{-1}$, and $2345\,cm^{-1}$ has not been detected after adsorption, as shown in Figure 3(c), analogous to that of OH. This is owing to the lone pair found in each bond stretch being filled with fluoride ions.

3.3.3. Thermogravimetric Analysis. The breakdown of cellulose, hemicellulose, and lignin, low molecular weight molecules such as carboxylic aldehydes, alkenes, and other components, are all linked to the thermal stability of materials during pyrolysis [1, 38]. High mass losses were detected in three degradation zones on the TGA curve of the biochar sample, as illustrated in Figures 4 (a) and (b). The release of water molecules caused the mass loss at 100°C [39]. Between 68°C and 273°C, there was a significant loss of mass, which might lead to the breakdown of low molecular weight molecules. Decomposition of larger molecular weight compounds resulted in a significant mass loss at 400°C. High mass losses were found at 450°C in the Teff straw biochar
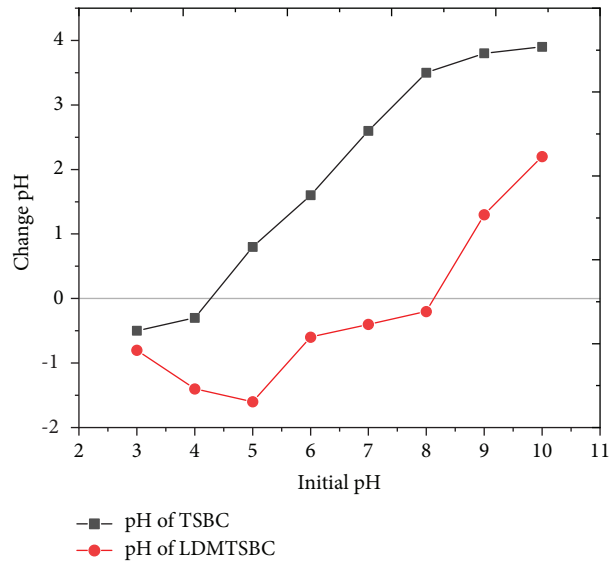
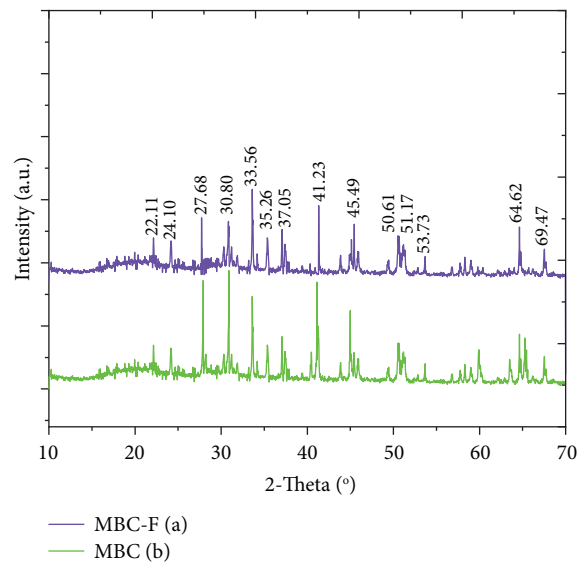FIGURE 1: Point zero charge determination for TSBC and LDMTSB.

FIGURE 2: X-ray patterns for lanthanum doped magnetic BC before and after defluoridation.

curve, as shown in Figure 4 (a). According to Figure 4(b), after 273°C, the mass loss is stable due to nanocomposite properties as well as the presence of metals within modified biochar [40]. The reduction of magnetite, hematite, and iron carbide composites into lower oxide groups, as shown in the above chemical process, maybe a concern during decomposition at higher temperatures. The catalytic actions of iron species on the carbon surface are predicted to cause the magnetic composite to decompose rapidly at higher temperatures [41].

3.3.4. Analysis for TSBC and LDMTSB.
The SEM pictures in Figures 5(a) and 5(b) clearly show the difference in biochar morphology before and after metal oxide nanoparticle modification. The heterogeneous layer with a high

micromere structure was shown by SEM morphology studies [42]. In contrast, the LDMTSB SEM picture in Figure 5(b) showed a rough and white surface. In addition, while comparing raw Teff straw biochar with lanthanum doped magnetic biochar, many tiny holes were discovered. The actions of metal oxide nanoparticles on the surface of biochar cause this morphological modification [43]. The development of pores on the LDMTSB adsorbent might explain the increase in surface area. Similar morphological structures have been reported in different previous researches [43, 44].

3.4. The Initial and Final Concentration of Fluoride Ion.
According to Haji et al.[3], the fluoride ions content in the Rift Valley region was higher than the WHO drinking water
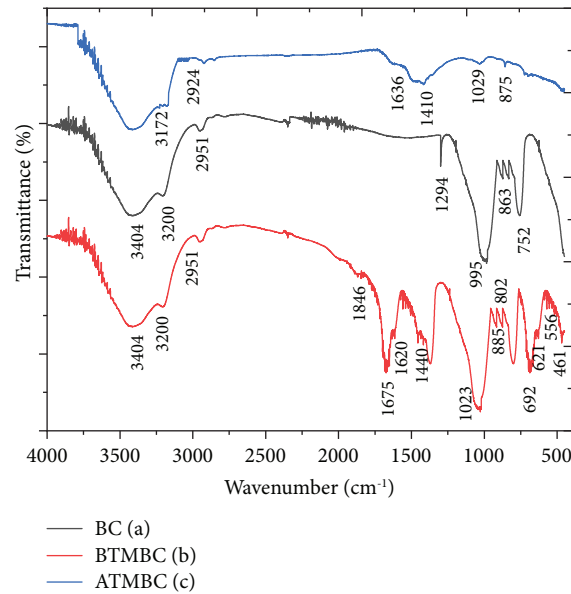
FIGURE 3: FTIR analysis for biochar, modified Teff straw biochar, and modified biochar treatment.
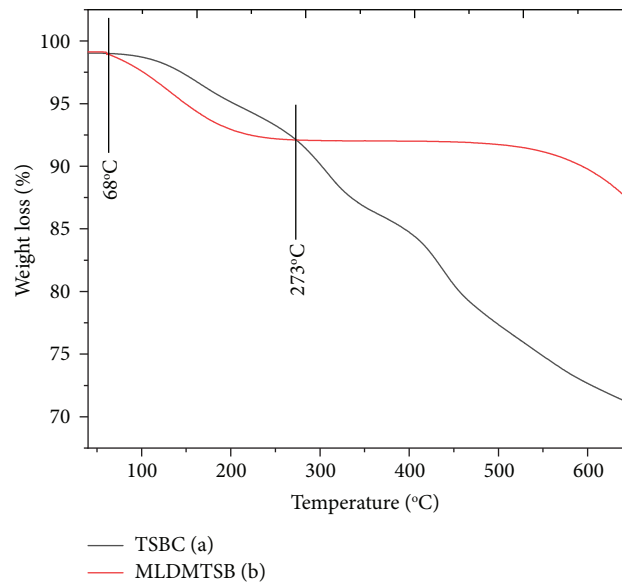

FIGURE 4: Thermogravimetric analysis of Teff straw biochar and lanthanum doped magnetic Teff straw biochar.

recommendation. As a result, treatment was required to lower the concentration of fluoride ions in groundwater and other sources of water with high fluoride content. The groundwater utilized in this study has a fluoride concentration of 56.2 mg/L and was sourced from the Rift Valley, especially Hawassa and Zeway city. The Rift Valley underground water has the following anions and cations, namely magnesium (Mg^{2+}), sodium (Na^+), potassium (K^+), calcium (Ca^{2+}), sulfate (SO_4^{2-}), bicarbonate (HCO_3^-), nitrates (NO_3^-) silica (SiO_2), chlorine (Cl^-), and fluoride (F^-) [3]. The blank solution was prepared from magnesium (Mg^{2+}), sodium (Na^+), potassium (K^+), calcium (Ca^{2+}), sulfate (SO_4^{2-}),

bicarbonate (HCO_3^-), nitrates (NO_3^-) silica (SiO_2), and chlorine (Cl^-) ions based on their concentration in groundwater. The stock fluoride concentration absorbance experiment was to create a standard curve. The absorbance of fluoride ions was measured using AAS. The concentration versus absorbance standard curve for fluoride ions was prepared, and this helps to determine the final concentration of fluoride ions after treatment. AAS was used to assess the absorbance capacity of the centrifuged solution. The standard curve was used to calculate the residual concentration of fluoride ions [45]. Equation (4) was used to compute the % elimination of fluoride ions.
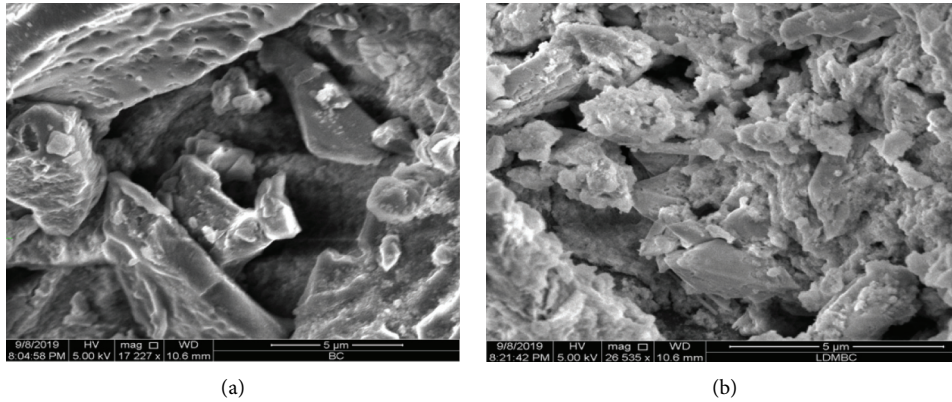
(a)

(b)

Figure 5: (a) SEM analysis of biochar and (b) lanthanum doped magnetic Teff straw biochar.

$$R\,(\%) = \frac{C_o - C_t}{C_o}, \qquad (8)$$

where R (%) denotes the proportion of removal percent, the starting concentration of fluoride ions is denoted by C_o, while the concentration of methyl orange after adsorption is denoted by C_t.

3.5. Defluoridation Process and Response Surface Methodology Analysis.

The response surface approach for the central composite design matrix is given in Table 1. The number of variables is four, and the total number of experiments is thirty, according to equation (6). The factorial design, the axial run, and the central run are the three primary elements of this experiment. The factorial design is made up of 16 experiments represented by 2^4, the axial run is made up of 8 experiments represented by 2×4, and the center run is made up of 6 experiments. The four independent variables are Dosage LDMTSB (g/L), Contact Time (min.), Rotational Speed (rpm), and pH; they were investigated to calculate the defluoridation effectiveness based on the laboratory experiment presented in Table 1. The coded variables A, B, C, and D stood for LDMTSB dosage (g/L), Contact Time (min.), Rotational Speed (rpm), and pH, respectively.

The data in Table 4 were evaluated using analysis of variance (ANOVA) with a significance threshold of 5% (α-value = 5%). In addition, the F-value and p value for models are provided in Table 4. The p value aids in determining the significance and nonsignificant of each factor, as well as the interaction component, which was adequately represented [46]. Dosage LDMTSB (A), contact time (B), rotational speed (C), and pH (D) were all significantly affecting the adsorption efficiency; thus, p values were less than 0.0001. BC, CD, BD, A^2, C^2, B^2, and D^2 have a substantial influence on adsorption efficiency as well as other interaction effects such as AB, AD, and AC because it has a p value that is higher than the α-value. The Model F-value of 66.19 indicates that the model is statistically significant. The F-value having a magnitude of 0.01 percent has a probability of occurring due to noise. According to Mustefa Beyan et al. [47], the sum of squares and F-value provide information about whether factors have a substantial negative or positive

impact on the response. The sum of squares and F-value are presented in Table 4. Single variables of dose, contact time, rotating speed, and pH had sums of square values of 805.51, 184.37, 60.67, and 121.59, respectively. Dosage, contact duration, rotating speed, and pH, all had F-values of 363.80, 83.27, 27.40, and 54.92, respectively. The model's sum of squares and F-value were 2051.75 and 66.19, respectively. According to this data, the dose has a substantial impact on defluoridation capability, followed by dosage, contact time, pH, and rotating speed. Aside from that, this experiment's lack-of-fit model is 0.9565. This means that the error terms do not influence the adsorption efficiency. The p value was smaller than the level of significance (α -value). Thus, the models were approved [48].

Standard deviation, mean, CV (%), R^2, adjusted R^2, projected R^2, and adequacy precision were analyzed by ANOVA are shown in Table 5 to fit statistical data. 1.49, 85.59, 1.74, 0.9841, 0.9692, 0.9520, and 26.7531 were the values for standard deviation, mean, C.V. (%), R^2, adjusted R^2, projected R^2, and adequate precision, respectively. According to Abeto Amibo [46], the adjusted and predicted R^2 are in good agreement below a 20% variation. The adjusted square of R (R^2) value was 0.9692. This indicates that it is reasonably close to the predicted square of R (R^2) value of 0.9520. Hence, the difference is less than 0.2. The signal-to-noise ratio is measured by adequacy precision [49]. It is preferable to have a ratio of more than four. The ratio for this model was 26.753 showing that the signal is adequate. The design space may be navigated using this paradigm. The proposed model for this study was quadratic; the coefficient of variation (CV) and standard deviation (SD) values were low and acceptable, with good agreements [50, 51]. The R^2 is approaching one, and the experimental and predicted values are well aligned. The outcomes for this analysis were close to 1, indicating that the data fit well and were highly acceptable.

In Table 6, the coefficients for every single factor and interaction effects are shown. The coefficients for Dosage LDMTSB (A), contact time (B), rotational speed (C), and pH (D) were 5.79, 2.77, 1.59, and -2.25. From their values, dosage LDMTSB (A), contact time (B), and rotational speed (C) had a positive relation with adsorption efficiency, but pH had a negative relation with the adsorption of fluoride ions.

TABLE 4: Analysis of variance (ANOVA) results.

Source	Sum of square	Df	Mean square	F-value	p value	
Model	2051.75	14	146.55	66.19	<0.0001	Significant
A: dosage LDMTSB	805.51	1	805.51	363.80	<0.0001	
B: contact time	184.37	1	184.37	83.27	<0.0001	
C: rotational speed	60.67	1	60.67	27.40	0.0001	
D: pH	121.59	1	121.59	54.92	<0.0001	
AB	0.1640	1	0.1640	0.0741	0.7892	
AC	0.9801	1	0.9801	0.4427	0.5159	
AD	0.2970	1	0.2970	0.1342	0.7193	
BC	56.18	1	56.18	25.37	0.0001	
BD	9.67	1	9.67	4.37	0.0500	
CD	58.91	1	58.91	26.60	0.0001	
A^2	386.19	1	386.19	174.42	<0.0001	
B^2	271.91	1	271.91	122.81	<0.0001	
C^2	77.17	1	77.17	34.85	<0.0001	
D^2	296.85	1	296.85	134.07	<0.0001	
Residual	33.21	15	2.21			
Lack of fit	12.08	10	1.21	0.2857	0.9565	Not significant
Pure error	21.14	5	4.23			
Cor total	2084.96	29				

The adsorption efficiency rises proportionately when the three variables, namely, dose, LDMTSB, contact duration, and rotating speed, increase. The relationship is reversed for pH. As the weight of the dose increases, more pores or adsorption sites become available, resulting in a more efficient and effective adsorption process. It is very obvious that increasing LDMTSB dosage would stream more available active sites for fluoride ions [52]. The adsorption process increased proportionately as the contact time increased because the fluoride ions had enough time to attach to the functional groups contained within the adsorbents [50]. Because the spinning magnetic stirrer avoids the sedimentation of adsorbents during the adsorption process, the rotational speed increases during the adsorption process in tandem with time and dose. The attraction of intermolecular interactions between molecules is referred to as Van der Waals forces [53]. According to Beyan et al. [54], the pH increase, and the adsorption process decrease, the pH decrease, and the adsorption capacity increase due to Van der Waals force present due to hydrogen bonds when the pH is

lower, and acidic medium. When all other factors are maintained constant, the coefficient estimate indicates the predicted change in response per unit change in factor value. In an orthogonal design, the intercept is the overall average response of all the runs [55]. The coefficients are changed depending on the factor settings around that average. When the factors are orthogonal, the VIFs are 1; when the factors are not orthogonal, the VIFs are larger than 1, indicating multicolinearity; the higher the VIF, the more severe the factor correlation. VIFs of fewer than ten are considered acceptable [56]. Table 6 shows that parameters such as LDMTSB dose (A), contact duration (B), rotating speed (C), and interaction effects like BC and CD all had a beneficial impact on defluoridation efficiency. Defluoridation efficiency was harmed by factors such as pH and interaction effects such as BD, D^2, C^2, B^2, and A^2. Based on Table 6, the model equation was developed to represent the defluoridation effectiveness by using coded variables in the following equation:

$$DF(\%) = 95.09 + 5.79A + 2.77B + 1.59C - 2.25D + 1.87Bc - 0.7775BD + 1.92CD - 3.75A^2 - 3.15B^2 - 1.68C^2 - 3.29D^2.$$

(9)

3.6. The Response's Actual vs. Predicted values. Figure 6 illustrates the actual and predicted values of defluoridation capacity, which were calculated by combining each independent variable. Figure 6 depicts the actual and predicted adsorption efficiency values. In this graph, the real and anticipated values are closely aligned, with an R^2 value of 0.9841. The difference between the real experimental values and the predicted fit value is represented by this R^2 value.

3.7. The 3D Diagram of Defluoridation Efficiency. A 3D representation of the adsorption of fluoride ions is shown in Figures 7(a) to 7(f). The adsorption results obtained in the 3D representation ranged from 69.75% to 97.95%. The maximum adsorption achieved was 97.95 percent in the 3D representation of Figures 7(a) to 7(f). The maximum yield was obtained at a dosage of 4 g, contact time of 60, a rotational speed of 600, and pH of 3. The difference

TABLE 5: Values for statistics of the fitting.

Values for statistics of fitting	
Std. dev.	1.49
Mean	85.59
CV %	1.74
R^2	0.9841
Adjusted R^2	0.9692
Predicted R^2	0.9520
Adeq precision	26.7531

TABLE 6: Coefficients of the coded variable.

| Factor	Coefficient estimate	D1f	Standard error	95% CI low	95% CI high	VIF
Intercept	95.09	1	0.6075	93.79	96.38	
A-dosage LDMTSB	5.79	1	0.3037	5.15	6.44	1.0000
B-contact time	2.77	1	0.3037	2.12	3.42	1.0000
C-rotational speed	1.59	1	0.3037	0.9426	2.24	1.0000
D-pH	−2.25	1	0.3037	−2.90	−1.60	1.0000
AB	−0.1013	1	0.3720	−0.8941	0.6916	1.0000
AC	0.2475	1	0.3720	−0.5454	1.04	1.0000
AD	−0.1362	1	0.3720	−0.9291	0.6566	1.0000
BC	1.87	1	0.3720	1.08	2.67	1.0000
BD	−0.7775	1	0.3720	−1.57	0.0154	1.0000
CD	1.92	1	0.3720	1.13	2.71	1.0000
A^2	−3.75	1	0.2841	−4.36	−3.15	1.05
B^2	−3.15	1	0.2841	−3.75	−2.54	1.05
C^2	−1.68	1	0.2841	−2.28	−1.07	1.05
D^2	−3.29	1	0.2841	−3.90	−2.68	1.05
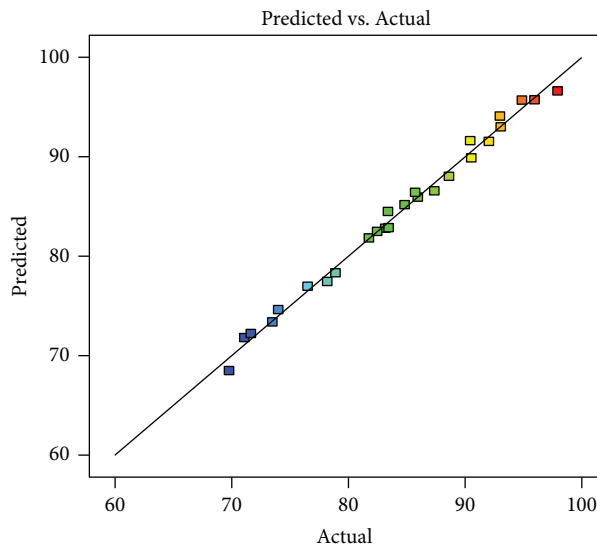
FIGURE 6: Actual versus predicted values for defluoridation efficiency.

between the shapes of the graph in Figures 7(a) and 7(f) was the changing and constant variables during the experiments.

3.8. Optimization of the Defluoridation Process. From Table 7, the optimized results for the defluoridation capacity of the adsorbent were analyzed. For optimization purposes, all independent variables were set in a range its importance was assigned by number 3, and the dependent variable was set at a maximum point that represented the importance of number 5 [46, 47]. The optimum results were 98.89%, and these results were obtained at a dosage of 3.97 g, contact time of 56.36 min, a rotational speed of 591.19 rpm, and pH of 3.968. To cross check these results, the experiment was done three times to testify the maximum adsorption of fluoride
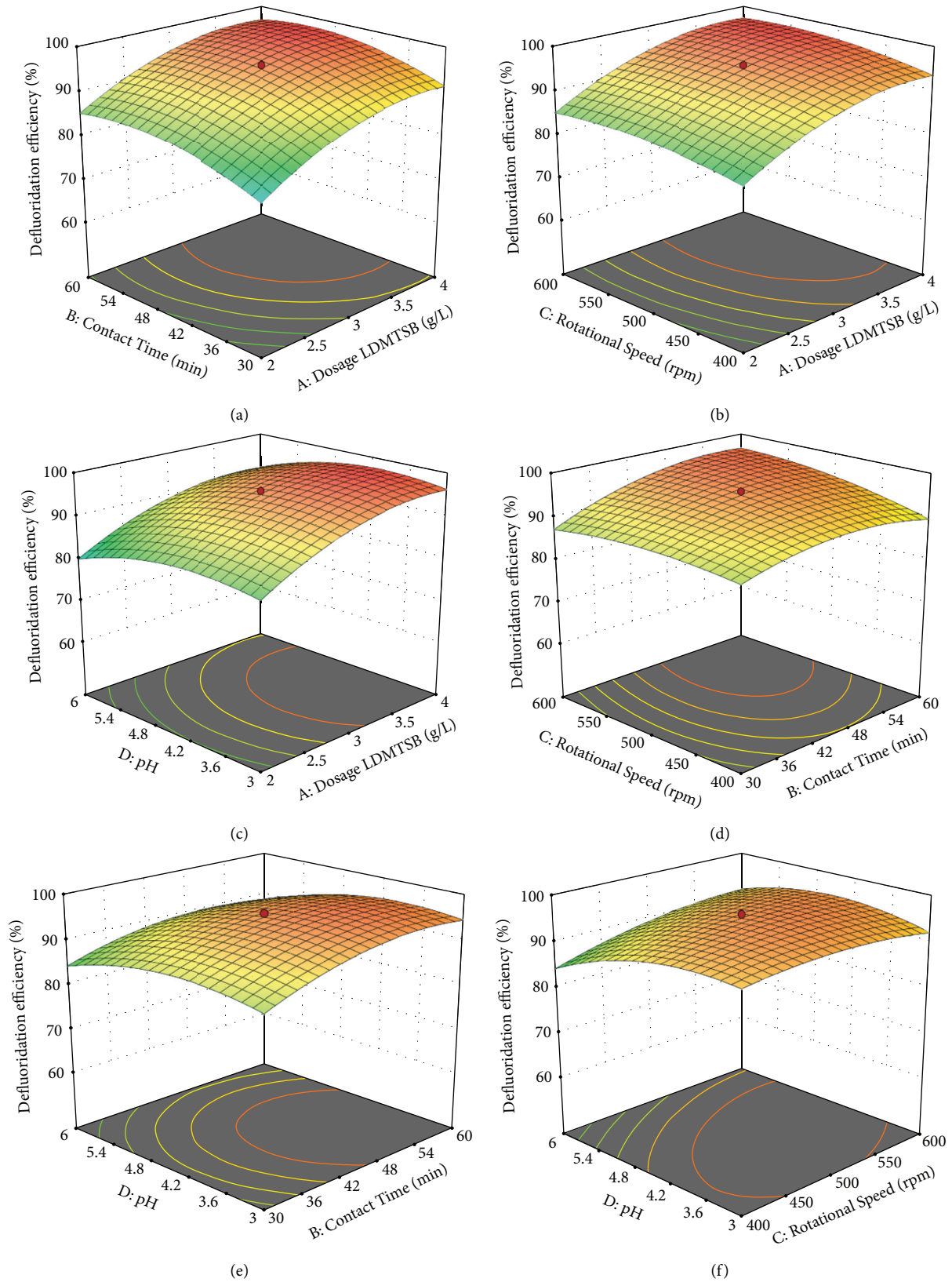
(a)

(b)

(c)

(d)

(e)

(f)

FIGURE 7: The 3D representation of defluoridation efficiency (%) by varying (a) contact time and dosage, (b) rpm and dosage, (c) pH and dosage, (d) rpm and time, (e) pH and contact time, (f) pH and rpm.

TABLE 7: Optimized results for the defluoridation process.

Name	Goal	Lower limit	Upper limit	Optimized results	Importance
A: dosage LDMTSB	is in range	2	4	3.567	3
B: contact time	is in range	30	60	56.36	3
C: rotational speed	is in range	400	600	591.19	3
D: pH	is in range	3	6	3.968	3
Defluoridation efficiency	Maximize	69.75	97.95	98.885	5
Desirability	Maximize	0	1	1	

ions from the solution. The experiments were conducted at a dosage of 3.97 g, contact time of 56.40 min, a rotational speed of 591.00 rpm, and pH of 3.97. In this case, the adsorption efficiency for fluoride ions was 98.85%. This result had almost the same results as the optimized results obtained from numerical optimization, but only the deviation was less than 0.04%. The desirability for this analysis was 1, and it is a good and highly acceptable model.

4. Conclusions

An efficient and novel LDMTSB adsorbent was synthesized and applied for the removal of fluoride ions in groundwater of Rift Valley located in Hawassa, Ethiopia. In this research, the following information was obtained, (I) Teff straw has 14.53% of fixed carbon, and this makes it an important candidate for biochar preparation. (II) At a dose: 3.57 g, adsorption time: 56.40 min, a rotating speed: 591.00 rpm, and a pH: 3.97, the optimal defluoridation (98.89%) was obtained, and its desirability was 1, (III) LDMTSB had hydroxyl, carbon-carbon double bond, and carbon-nitrogen triple bond, and these functional groups facilitate adsorption of fluoride ions, (IV) in comparison with TSBC and LDMTSB nanocomposite, the later exhibits great thermal stability at high temperatures and has a better ability for removing fluoride ions from water and (V) the surface areas of TSB and LDMTSB were 120.61 and 321.52 m^2/g, respectively.

Data Availability

The data used to support the findings of this study are included in the article.

Conflicts of Interest

The authors declare that they have no conflicts of interest.

References

[1] B. Toussaint, B. Raffael, A. Angers-Loustau et al., "Review of micro- and nanoplastic contamination in the food chain," *Food Additives & Contaminants: Part A*, vol. 36, no. 5, pp. 639–673, 2019.

[2] K. H. Vardhan, P. S. Kumar, and R. C. Panda, "A review on heavy metal pollution, toxicity and remedial measures: current trends and future perspectives," *Journal of Molecular Liquids*, vol. 290, Article ID 111197, 2019.

[3] M. Haji, D. Wang, L. Li, D. Qin, and Y. Guo, "Geochemical evolution of fluoride and implication for F– enrichment in groundwater: example from the bilate river basin of southern main Ethiopian rift," *Water*, vol. 10, no. 12, 2018.

[4] G. Singh, B. Kumari, G. Sinam, Kriti, N. Kumar, and S. Mallick, "Fluoride distribution and contamination in the water, soil and plants continuum and its remedial technologies, an Indian perspective- a review," *Environmental Pollution*, vol. 239, pp. 95–108, 2018.

[5] I. Mukherjee and U. K. Singh, "Groundwater fluoride contamination, probable release, and containment mechanisms: a review on Indian context," *Environmental Geochemistry and Health*, vol. 40, no. 6, pp. 2259–2301, 2018.

[6] A. Maleki and H. Jari, "Evaluation of drinking water quality and non-carcinogenic and carcinogenic risk assessment of heavy metals in rural areas of Kurdistan, Iran," *Environmental Technology & Innovation*, vol. 23, Article ID 101668, 2021.

[7] O. Akoto, J. A. Teku, and D. Gasinu, "Chemical characteristics and health hazards of heavy metals in shallow groundwater: case study Anloga community, Volta Region, Ghana," *Applied Water Science*, vol. 9, no. 2, p. 36, 2019.

[8] M. Vithanage and P. Bhattacharya, "Fluoride in the environment: sources, distribution and defluoridation," *Environmental Chemistry Letters*, vol. 13, no. 2, pp. 131–147, 2015.

[9] A. W. Wagutu, R. Machunda, and Y. A. C. Jande, "Crustacean derived calcium phosphate systems: application in defluoridation of drinking water in East African rift valley," *Journal of Hazardous Materials*, vol. 347, pp. 95–105, 2018.

[10] H. D. Beyene, N. G. Habtu, and A. Ayalew, "Removal of methylene blue dye from textile wastewater using activated carbon prepared from rice husk," *International Journal of Innovation Science and Research*, vol. 9, no. 2, pp. 317–325, 2014.

[11] M. H. Mahmoudian, M. Fazlzadeh, M. H. Niari, A. Azari, and E. C. Lima, "A novel silica supported chitosan/glutaraldehyde as an efficient sorbent in solid phase extraction coupling with HPLC for the determination of Penicillin G from water and wastewater samples," *Arabian Journal of Chemistry*, vol. 13, no. 9, pp. 7147–7159, 2020.

[12] Y. Rashtbari, S. Hazrati, A. Azari, S. Afshin, M. Fazlzadeh, and M. Vosoughi, "A novel, eco-friendly and green synthesis of PPAC-ZnO and PPAC-nZVI nanocomposite using pomegranate peel: cephalexin adsorption experiments, mechanisms, isotherms and kinetics," *Advanced Powder Technology*, vol. 31, no. 4, pp. 1612–1623, 2020.

[13] A. Azari, R. Nabizadeh, A. H. Mahvi, and S. Nasseri, "Integrated Fuzzy AHP-TOPSIS for selecting the best color removal process using carbon-based adsorbent materials: multi-criteria decision making vs. systematic review approaches and modeling of textile wastewater treatment in real conditions," *International Journal of Environmental Analytical Chemistry*, pp. 1–16, 2020.

[14] S. Bolognesi, G. Bernardi, A. Callegari, D. Dondi, and A. G. Capodaglio, "Biochar production from sewage sludge and microalgae mixtures: properties, sustainability and

possible role in circular economy," *Biomass Conversion and Biorefinery*, vol. 11, no. 2, pp. 289–299, 2021.

[15] T. F. Rittl, K. Butterbach-Bahl, C. M. Basile et al., "Greenhouse gas emissions from soil amended with agricultural residue biochars: effects of feedstock type, production temperature and soil moisture," *Biomass and Bioenergy*, vol. 117, pp. 1–9, 2018.

[16] M. Fazeli Sangani, S. Abrishamkesh, and G. Owens, "Physicochemical characteristics of biochars can be beneficially manipulated using post-pyrolyzed particle size modification," *Bioresource Technology*, vol. 306, Article ID 123157, 2020.

[17] K. A. Mottaleb and D. B. Rahut, "Household production and consumption patterns ofTeffin Ethiopia," *Agribusiness*, vol. 34, no. 3, pp. 668–684, 2018.

[18] A. B. Bageru and V. C. Srivastava, "Biosilica preparation from abundantly available African biomass teff (Eragrostis tef) straw ash by sol-gel method and its characterization," *Biomass Conversion and Biorefinery*, vol. 8, no. 4, pp. 971–978, 2018.

[19] D. Huang, Q. Zhang, C. Zhang et al., "Mn doped magnetic biochar as persulfate activator for the degradation of tetracycline," *Chemical Engineering Journal*, vol. 391, Article ID 123532, 2020.

[20] Y. Wu, D. Li, J. Lu et al., "LaMnO3-La2CuO4 two-phase synergistic system with broad active window in NOx efficient reduction," *Molecular Catalysis*, vol. 493, Article ID 111111, 2020.

[21] A. Azari, R. Nabizadeh, A. H. Mahvi, and S. Nasseri, "Magnetic multi-walled carbon nanotubes-loaded alginate for treatment of industrial dye manufacturing effluent: adsorption modelling and process optimisation by central composite face-central design," *International Journal of Environmental Analytical Chemistry*, pp. 1–21, 2021.

[22] A. Azari, M. Yeganeh, M. Gholami, and M. Salari, "The superior adsorption capacity of 2,4-Dinitrophenol under ultrasound-assisted magnetic adsorption system: modeling and process optimization by central composite design," *Journal of Hazardous Materials*, vol. 418, Article ID 126348, 2021.

[23] R. Deng, D. Huang, J. Wan et al., "Chloro-phosphate impregnated biochar prepared by co-precipitation for the lead, cadmium and copper synergic scavenging from aqueous solution," *Bioresource Technology*, vol. 293, Article ID 122102, 2019.

[24] S. H. Dhawane, S. Chowdhury, and G. Halder, "Lipase immobilised carbonaceous catalyst assisted enzymatic transesterification of Mesua ferrea oil," *Energy Conversion and Management*, vol. 184, pp. 671–680, 2019.

[25] C. Tongcumpou, P. Usapein, and N. Tuntiwiwattanapun, "Complete utilization of wet spent coffee grounds waste as a novel feedstock for antioxidant, biodiesel, and bio-char production," *Industrial Crops and Products*, vol. 138, Article ID 111484, 2019.

[26] J. J. Ojeda and M. Dittrich, "Fourier transform infrared spectroscopy for molecular analysis of microbial cells," *Microbial Systems Biology*, vol. 881, pp. 187–211, 2012.

[27] W. Yao, Y. Weng, and J. M. Catchmark, "Improved cellulose X-ray diffraction analysis using Fourier series modeling," *Cellulose*, vol. 27, no. 10, pp. 5563–5579, 2020.

[28] P. Karthikeyan, S. Vigneshwaran, and S. Meenakshi, "Removal of phosphate and nitrate ions from water by amine crosslinked magnetic banana bract activated carbon and its physicochemical performance," *Environmental Nanotechnology, Monitoring & Management*, vol. 13, Article ID 100294, 2020.

[29] M. Khraisheh, K. M. Zadeh, A. I. Alkhouzaam et al., "Characterization of polysulfone/diisopropylamine 1-alkyl-3-methylimidazolium ionic liquid membranes: high pressure gas separation applications," *Greenhouse Gases: Science and Technology*, vol. 10, no. 4, pp. 795–808, 2020.

[30] L. Kong, Y. Tian, Z. Pang et al., "Synchronous phosphate and fluoride removal from water by 3D rice-like lanthanum-doped La@MgAl nanocomposites," *Chemical Engineering Journal*, vol. 371, pp. 893–902, 2019.

[31] W. S. Saeed, A.-B. Al-Odayni, A. Ali Alghamdi, A. Abdulaziz Al-Owais, A. Semlali, and T. Aouak, "Miscibility of poly(-ethylene-co-vinylalcohol)/poly(δ-valerolactone) blend and tissue engineering scaffold fabrication using naphthalene as porogen," *Polymer-Plastics Technology and Materials*, vol. 58, no. 2, pp. 1–23, 2019.

[32] M. I. Ejimofor, I. G. Ezemagu, and M. C. Menkiti, "Physiochemical, Instrumental and thermal characterization of the post coagulation sludge from paint industrial wastewater treatment," *South African Journal of Chemical Engineering*, vol. 37, pp. 150–160, 2021.

[33] J. Liu, Q.-h. Zhang, F. Ma, S.-f. Zhang, Q. Zhou, and A.-m. Huang, "Three-step identification of infrared spectra of similar tree species to Pterocarpus santalinus covered with beeswax," *Journal of Molecular Structure*, vol. 1218, Article ID 128484, 2020.

[34] S. G. Prasad, A. De, and U. De, "Structural and optical investigations of radiation damage in transparent PET polymer films," *International Journal of Spectroscopy*, vol. 2011, Article ID 810936, 2011.

[35] S. Dawood, T. K. Sen, and C. Phan, "Synthesis and characterization of slow pyrolysis pine cone bio-char in the removal of organic and inorganic pollutants from aqueous solution by adsorption: kinetic, equilibrium, mechanism and thermodynamic," *Bioresource Technology*, vol. 246, pp. 76–81, 2017.

[36] S. J. Gerber and E. Erasmus, "Electronic effects of metal hexacyanoferrates: an XPS and FTIR study," *Materials Chemistry and Physics*, vol. 203, pp. 73–81, 2018.

[37] T. Chi, J. Zuo, and F. Liu, "Performance and mechanism for cadmium and lead adsorption from water and soil by corn straw biochar," *Frontiers of Environmental Science & Engineering*, vol. 11, no. 2, p. 15, 2017.

[38] H. Durak, S. Genel, and M. Tunç, "Pyrolysis of black cumin seed: significance of catalyst and temperature product yields and chromatographic characterization," *Journal of Liquid Chromatography & Related Technologies*, vol. 42, no. 11-12, pp. 331–350, 2019.

[39] Y. Li, C. Jia, X. Zhang et al., "Synthesis and performance of bio-based epoxy coated urea as controlled release fertilizer," *Progress in Organic Coatings*, vol. 119, pp. 50–56, 2018.

[40] M. T. H. Siddiqui, H. Ahmed Baloch, S. Nizamuddin et al., "Synthesis of novel magnetic carbon nanocomposite from waste biomass: a comparative study of industrially adoptable hydro/solvothermal co-precipitation route," *Journal of Environmental Chemical Engineering*, vol. 8, no. 2, Article ID 103519, 2020.

[41] M.-H. Li, K.-Y. A. Lin, M.-T. Yang, B. X. Thanh, and D. C. W. Tsang, "Prussian Blue Analogue-derived co/fe bimetallic nanoparticles immobilized on S/N-doped carbon sheet as a magnetic heterogeneous catalyst for activating peroxymonosulfate in water," *Chemosphere*, vol. 244, Article ID 125444, 2020.

[42] B. Armynah, D. Tahir, M. Tandilayuk, Z. Djafar, and W. H. Piarah, "Potentials of biochars derived from bamboo leaf biomass as energy sources: effect of

temperature and time of heating," *International Journal of Biomaterials*, vol. 2019, 9 pages, 2019.

[43] B. Janković, N. Manić, and V. Dodevski, "Pyrolysis kinetics of poplar fluff bio-char produced at high carbonization temperature: a mechanistic study and isothermal life-time prediction," *Fuel*, vol. 296, Article ID 120637, 2021.

[44] J. Zhou, F. Ma, and H. Guo, "Adsorption behavior of tetracycline from aqueous solution on ferroferric oxide nanoparticles assisted powdered activated carbon," *Chemical Engineering Journal*, vol. 384, Article ID 123290, 2020.

[45] C. A. Canciam and N. C. Pereira, "Assessment of the use of epicarp and mesocarp of green coconut for removal of fluoride ions in aqueous solution," *International Journal of Chemical Engineering*, vol. 2019, 8 pages, 2019.

[46] T. Abeto Amibo, "Modeling and pulping variables optimization OF ethanol-alkali pulping and delignification OF grevillea robusta IN Ethiopia BY response surface methodology," *European Journal of Materials Science and Engineering*, vol. 6, no. 1, pp. 34–51, 2021.

[47] S. Mustefa Beyan, S. Venkatesa Prabhu, T. K. Mumecha, and M. T. Gemeda, "Production of alkaline proteases using Aspergillus sp. isolated from injera: RSM-GA based process optimization and enzyme kinetics aspect," *Current Microbiology*, vol. 78, no. 5, pp. 1823–1834, 2021.

[48] T. A. Amibo and A. B. Bayu, "Calcium carbonate synthesis , optimization and characterization from egg," *International Journal of Modern Science and Technology*, vol. 5, 2020.

[49] T. K. Mumecha, B. Surafel Mustefa, S. Venkatesa Prabhu, and F. T. Zewde, "Alkaline protease production using eggshells and membrane-based substrates: process modeling, optimization, and evaluation of detergent potency," *Engineering and Applied Science Research*, vol. 48, no. 2, pp. 171–180, 2021.

[50] Y. Asrat, A. T. Adugna, M. Kamaraj, and S. M. Beyan, "Adsorption phenomenon of arundinaria alpina stem-based activated carbon for the removal of lead from aqueous solution," *Journal of Chemistry*, vol. 2021, pp. 1–9, Article ID 5554353, 2021.

[51] P. S. Venkatesa, G. Girma, A. K. Gizachew, M. Surafel, M. Beyan, and G. Ramesh, "Biosolubilization of Cr (VI) from tannery sludge: process modeling, optimization, rate kinetics and thermodynamics aspects," *International Journal of Recent Technology and Engineering*, vol. 8, no. 4, pp. 4808–4816, 2019.

[52] J. Wang, N. Chen, M. Li, and C. Feng, "Efficient removal of fluoride using polypyrrole-modified biochar derived from slow pyrolysis of pomelo peel: sorption capacity and mechanism," *Journal of Polymers and the Environment*, vol. 26, no. 4, pp. 1559–1572, 2018.

[53] W. Kidus Tekleab, S. M. Beyan, S. Balakrishnan, and H. Admassu, "Chicken feathers based Keratin extraction process data analysis using response surface-box-Behnken design method and characterization of keratin product," *Current Applied Science and Technology*, vol. 20, no. 2, pp. 163–177, 2020.

[54] S. M. Beyan, S. V. Prabhu, T. T. Sissay, and A. A. Getahun, "Sugarcane bagasse based activated carbon preparation and its adsorption efficacy on removal of BOD and COD from textile effluents: RSM based modeling, optimization and kinetic aspects," *Bioresource Technology Reports*, vol. 14, Article ID 100664, 2021.

[55] D. A. A. Abreham Bekele Bayu, "Conversion of degradable municipal solid waste into fuel briquette: case of Jimma city municipal solid waste," *Iranian Journal of Energy and Environment*, vol. 11, no. 2, 2020.

[56] K. Umanath, K. Palanikumar, V. Sankaradass, and K. Uma, "Optimization of wear properties on AA7075/Sic/Mos2 hybrid metal matrix composite by response surface methodology," *Materials Today: Proceedings*, vol. 46, pp. 4019–4024, 2021.